ACS APPLIED MATERIALS & INTERFACES

Research Article

www.acsami.org

Defect Evolution in Graphene upon Electrochemical Lithiation

Laila Jaber-Ansari,[†,○] Kanan P. Puntambekar,[†,○] Hadi Tavassol,[‡] Handan Yildirim,[§] Alper Kinaci,[∥] Rajan Kumar,[†] Spencer J. Saldaña,[⊥] Andrew A. Gewirth,[‡] Jeffrey P. Greeley,[§] Maria K. Y. Chan,[∥] and Mark C. Hersam*[,†,#,▽]

[†]Department of Materials Science and Engineering, Northwestern University, Evanston, Illinois 60208, United States

[‡]Department of Chemistry, University of Illinois at Urbana−Champaign, Urbana, Illinois 61801, United States

[§]School of Chemical Engineering, Purdue University, West Lafayette, Indiana 47907, United States

[∥]Center for Nanoscale Materials, Argonne National Laboratory, Argonne, Illinois 60439, United States

[⊥]Department of Chemical and Biological Engineering, Northwestern University, Evanston, Illinois 60208, United States

[#]Department of Chemistry, Northwestern University, Evanston, Illinois 60208, United States

[▽]Department of Medicine, Northwestern University, Chicago, Illinois 60611, United States

Supporting Information

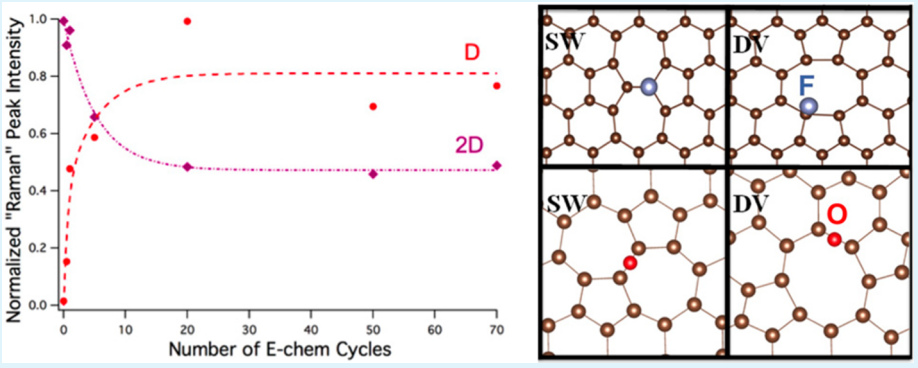

ABSTRACT: Despite rapidly growing interest in the application of graphene in lithium ion batteries, the interaction of the graphene with lithium ions and electrolyte species during electrochemical cycling is not fully understood. In this work, we use Raman spectroscopy in a model system of monolayer graphene transferred on a Si(111) substrate and density functional theory (DFT) to investigate defect formation as a function of lithiation. This model system enables the early stages of defect formation to be probed in a manner previously not possible with commonly used reduced graphene oxide or multilayer graphene substrates. Using ex situ and Ar-atmosphere Raman spectroscopy, we detected a rapid increase in graphene defect level for small increments in the number of lithiation/delithiation cycles until the I(D)/I(G) ratio reaches ∼1.5−2.0 and the 2D peak intensity drops by ∼50%, after which the Raman spectra show minimal changes upon further cycling. Using DFT, the interplay between graphene topological defects and chemical functionalization is explored, thus providing insight into the experimental results. In particular, the DFT results show that defects can act as active sites for species that are present in the electrochemical environment such as Li, O, and F. Furthermore, chemical functionalization with these species lowers subsequent defect formation energies, thus accelerating graphene degradation upon cycling. This positive feedback loop continues until the defect concentration reaches a level where lithium diffusion through the graphene can occur in a relatively unimpeded manner, with minimal further degradation upon extended cycling. Overall, this study provides mechanistic insight into graphene defect formation during lithiation, thus informing ongoing efforts to employ graphene in lithium ion battery technology.

KEYWORDS: *graphene, silicon, lithium ion battery, defects, Raman spectroscopy, density functional theory*

1. INTRODUCTION

Graphene and graphene-based composites have attracted significant attention as electrodes in lithium ion batteries.[1−8] For example, the high surface area and electron mobility of graphene result in rapid charge transport during electrochemical cycling, which makes it suitable for high-power battery applications.[9−11] Furthermore, the superlative mechanical strength and resilience of graphene sheets allows them to be utilized as a conducting support network for high-capacity materials, such as silicon, that undergo large volume changes during lithiation and delithiation.[11,12] In addition, the solid-electrolyte interphase (SEI) on graphene is similar to graphite,

Received: June 13, 2014
Accepted: September 29, 2014
Published: September 29, 2014

which is well-established in conventional lithium ion batteries and can be tuned by the appropriate choice of electrolyte.[13,14] Despite the substantial interest in this area, the interaction of graphene with lithium ions and electrolyte species during electrochemical cycling is not fully understood.

Lithium intercalation through graphene is commonly attributed to a defect-mediated process due to the high diffusion barrier of lithium ions through the pristine basal plane of graphene.[15−17] In particular, several theoretical studies show that Li ions are not likely to interact strongly with the basal plane of defect-free graphene and that chemisorption is only possible at defect sites.[18−21] Studies of lithium interaction and diffusion on graphene with topological defects such as Stone−Wales (SW), double vacancies (DV), and single vacancies (SV)[16,17,22] suggest attractive Li interaction with the vacancies, possibly enhancing Li adsorption.[16] Additionally, graphene functionalization with F, O, and H species have been of high interest.[23−27] However, the formation of defects upon Li adsorption to graphene, and the relationships between topological defects and functionalization with electrolyte-decomposition species, such as O and F, have not been previously studied.

Graphene films used in lithium ion batteries, especially for graphene-based composites, are commonly in the form of reduced graphene oxide (rGO),[28,29] which is a highly functionalized and defective form of graphene.[30] Thus, the early stages of defect formation in graphene during electrochemical cycling cannot be observed in such cases due to the high background defect concentration level. In contrast, we use a monolayer film of graphene (with less than 20% bilayer islands) grown by chemical vapor deposition (CVD) in order to observe the early stage defects. This method yields monolayer graphene with low defect density (i.e., low Raman defect peak intensity) over large areas that can be transferred to arbitrary substrates.[31]

Raman spectroscopy has been extensively used for characterizing graphene.[32] Specifically, it probes the effects of deformation such as tensile and compressive strain,[33,34] as well as physical and chemically induced defects such as vacancies and chemical functionalization.[35−37] However, previous reports of Raman characterization of electrochemically lithiated graphene have been on silicon oxide[38] and copper[39] that show minimal or no lithiation. On the other hand, we choose single crystal Si(111) substrates due to their high lithium capacity,[29,40,41] enabling significant lithium intercalation through the graphene that has been transferred on the Si(111) surface. The ultraflat surface of Si(111) also facilitates uniform transfers of the monolayer graphene film over large areas and thus is amenable to surface-sensitive characterization.

Using Raman spectroscopy, we show a systematic evolution of the defectivity in a single-layer CVD graphene film on Si(111) as a function of electrochemical cycling. In the early stages of defect evolution, a rapid increase in graphene defect level is detected for small increments in the number of lithiation/delithiation cycles until the I(D)/I(G) ratio reaches ∼1.5−2.0 and the 2D peak intensity drops by ∼50%, after which subsequent lithiation shows minimal changes in the Raman spectra. A corresponding density functional theory (DFT) study explores the interplay between graphene topological defects and chemical functionalization in order to provide insight into the experimental results. For example, DFT shows that graphene defects can act as active sites for adsorbates (Li, O, and F) and that this chemical functionalization lowers defect formation energies. In this respect, active sites with specific adsorbates act as nuclei for extended defects. However, the experimental results show that the defect formation does not continue indefinitely upon extended electrochemical cycling. Consequently, this positive feedback loop between defect formation and chemical functionalization is terminated at a certain point, possibly due to the exhaustion of new functionalization species upon completion of SEI formation.

2. EXPERIMENTAL AND COMPUTATIONAL METHODS

2.1. Sample Preparation. Monolayer graphene films were grown on Cu foil using chemical vapor deposition (CVD). Initially, 80 μm thick Cu foil was cleaned with acetone and isopropanol. The Cu foil was then electropolished in a 3:1 by volume mixture of H_3PO_4 (85%) and poly(ethylene glycol) at an applied voltage of 2.0 V for 30 min. After electropolishing, the residual acid on the Cu foil was neutralized using a 1% ammonia in water solution and rinsed with deionized water. The Cu foil was then placed in a CVD tube furnace and pumped down to ∼30−50 mTorr. An Ar/H_2 (4:1) gas mixture was used to flush the system, raising the total pressure to 100 mTorr. The temperature was then linearly increased to 1000 °C in 1 h. At 1000 °C, 10 sccm of methane was added, which increased the pressure to 300 mTorr. The sample was held at these conditions for 30 min, during which graphene growth occurred. After the growth step, the reactor was cooled to 800 °C in 15 min, and the methane flow was discontinued. The system was then allowed to rapidly cool to room temperature.

After CVD growth, the graphene on the back of the Cu foil was cleaned using reactive ion etching.[42] Poly(methyl methacrylate) (PMMA) was then spin coated on top of the Cu foil/graphene at 2000 rpm. The PMMA was left to dry on the sample for at least 6 h at room temperature. The Cu was subsequently etched in Marble's reagent (8 g of $CuSO_4$, 50 mL of H_2O, 50 mL of HCl) for ∼4 h. Once all of the Cu was etched from the film, the PMMA/graphene was rinsed three times using deionized water baths to remove any remaining Marble's reagent. The PMMA/graphene film was then gently transferred onto a Si(111) substrate with a surface native oxide. The Si(111) substrates were diced to 5 × 5 mm size, rinsed with isopropanol, and dried prior to the graphene transfer. The graphene films were sized larger than the silicon substrates to ensure that they wrapped around the edges of the Si on all sides. The samples were air-dried and then placed in a vacuum oven for 15 min at 115 °C and another 3 h at 65 °C to remove residual water from the transfer and improve graphene adhesion to the substrate. The samples were subsequently immersed in an acetone bath for at least 4 h, rinsed with acetone and isopropanol, and then annealed in an Ar/H_2 (4:1) gas mixture for 3 h at 350 °C to remove the PMMA.

2.2. Electrochemical Cycling. For ex situ characterization, the monolayer graphene-coated Si(111) substrates, henceforth referred to as "G-Si", were electrochemical cycled in a coin cell setup. In particular, the cycling was performed in MTI 314 stainless steel coin cells using lithium metal as the counter electrode and Celgard 2320 and Whatman glass fiber separators. The electrolyte was 1 M $LiPF_6$ (Novolyte) in 1:1 by volume ethylene carbonate and dimethyl carbonate (Novolyte, Sigma-Aldrich). All coin cells were galvanostatically cycled at a current of 35−40 × 10^{-6} A/cm^2 between 0.025 and 2 V using an Arbin BT2143 battery tester. A series of samples were generated at the first (0.5, 1, and 5 cycles) and second (20, 50, and 70 cycles) phase of electrochemical cycling. The 0.5 cycle sample was subjected to a single lithiation cycle from open circuit voltage to ∼100 mV. An example of the galvanostatic cycling is shown in Figure S1a (Supporting Information). The samples are henceforth referred to as "G-Si-x" or "x", where x indicates the number of cycles. For example, G-Si-5 or "5" will indicate the sample that has undergone 5 electrochemical cycles. Additionally, a 20 cycle bare Si(111) with no graphene coating was prepared in order to subtract the silicon background from the Raman spectra.

After cycling, the coin cells were opened in an Ar-filled glovebox with <1 ppm oxygen and moisture content to remove the G-Si substrates. The surface of the sample was rinsed with isopropanol to remove residual electrolyte and gently dried by placing upside down on a Kimwipe. The samples were then removed from the glovebox for ex situ Raman characterization.

For Ar atmosphere Raman measurements, the monolayer graphene film was transferred onto a Si(100) substrate with a 100 nm thick silicon oxide, henceforth referred to as "G-SiO_2" (Figure S2a, Supporting Information). The silicon oxide substrate was chosen to mitigate the signal loss due to the quartz window of the spectrochemical cell used for the Ar atmosphere Raman measurements and to minimize the lithiation effects of the substrate. For electrochemical cycling, cyclic voltammetry was performed using a CH Instruments potentiostat, between potentials of 2 and 20 mV vs Li/Li^+ for one and three cycles (Figure S2b, Supporting Information), using the same electrolyte system as the ex situ samples. After cycling, the samples were removed from the cell in an Ar filled glovebox, with <1 ppm oxygen and rinsed with acetonitrile to remove residual electrolyte. The samples were then assembled and sealed in a spectrochemical cell in the Ar filled glovebox and subsequently transferred in order to collect Raman spectra.

2.3. Characterization and Data Analysis. Ex situ Raman measurements were performed using a Renishaw inVia Confocal Raman Microscope. A 514 nm, 13.8 mW laser was used for the measurements at a 50× magnification (laser spot size ~2−3 μm in diameter) with accumulation times of up to 60 s to resolve the low intensity peaks. All of the scans were normalized with respect to the ambient N_2 peak at 2331 cm^{-1}. The silicon background in the Raman spectra was then subtracted from all the G-Si scans. Figure S3a (Supporting Information) shows the Raman spectrum of an electrochemically cycled Si(111) substrate that was used for the background subtraction. For each condition, the scans were averaged over 4−8 regions, and the averaged data were used for further analysis. Lorentzian peak fits were used for all the peaks, except D′ which was fit using a Voigt function. Peak heights obtained from the fits are used in the data analysis and referred to as "I(x)" in the following text. For the purpose of this study, the bilayer regions were not included in the Raman analysis. The bilayer islands can be identified by their distinct Raman spectra, which is different from monolayer graphene, as shown in Figure S2d (Supporting Information).

To ensure that the defects observed by Raman are not artifacts of coin cell crimping or rinsing of graphene after opening the coin cells, a control experiment was performed. In this experiment, a graphene sample on silicon dioxide was taken through all the steps of coin cell fabrication, opening, and rinsing. Figure S3d (Supporting Information) shows the Raman spectra of this sample before and after this procedure. Several spots were measured on the sample, and no location was found that indicated a significant increase in the defect peak.

2.4. Density Functional Theory (DFT). DFT calculations were performed using the Vienna Ab-Initio Simulation Package (VASP)[43] with accompanying Projector Augmented Wave (PAW) potentials.[44] The calculations were performed using an energy cutoff of 500 eV. The Perdew−Burke−Ernzerhof (PBE) exchange-correlation functional was used.[45] A 4 × 4 supercell model with 20 Å of vacuum was used for the calculations of Li, F, and O adsorption. A 3 × 3 supercell was also used for O calculations for supercell size dependence study and for strained graphene vibrational frequency calculations. A Γ-centered 6 × 6 × 1 k-point grid was also employed. The geometry optimization was achieved by using conjugate gradient minimization. Atomic positions were relaxed until the forces on each atom were smaller than 0.01 eV/Å. The calculations were spin-polarized.

For isolated Li and F adsorption on graphene, the total energy of the system was first evaluated with the adsorbate at the hollow (on top of hexagon), the bridge (in between C−C bonds), and the top (on top of C atom) sites. The most stable adsorption sites for isolated Li and F were found to be the hollow and top sites (on C), respectively. For introducing the second Li, only the adsorption on the available hollow sites was considered for both single and double side adsorptions. For the third Li, using the lowest energy configurations of the previous step, the adsorption on the hollow site for both single and double side adsorption was calculated. For higher F concentrations, on the other hand, in addition to the hollow site, we also included adsorption on bridge and top sites. To find adsorption sites for O, we considered positions forming a 5 × 5 grid on the graphene superlattice. The concentration of O was increased by keeping the most stable adsorbate position(s) at a given concentration and adding the next O from the pool of points that belong to 5 × 5 grids on both sides of graphene.

From the above sampling, we selected those configurations that have the lowest energy for each Li, F, and O content considered. The adsorption energy for an adatom, A, was calculated using the expression

$$E_{ads}{}^{A} = E^{A/G} - E^{G} - E^{A} \quad (1)$$

where $E^{A/G}$ is the total energy of graphene with the adsorbed atom, E^{G} is the energy of graphene, and E^{A} is the energy of the reference state for the adatom. For Li, the reference state energy was taken to be the energy of the bcc bulk Li.

For determining the adsorbate-induced change in defect formation energies, first, the formation energies of SW and DV defects were calculated using the formula

$$E_f{}^{d} = E^{G-d} - N\mu(C) \quad (2)$$

where $E^{G\text{-}d}$ is the total energy of graphene with defect, N is the number of atoms in defected graphene, and $\mu(C)$ is the chemical potential of C, which was calculated using the total energy of pristine graphene divided by the number of C atoms. The defect formation energy in the presence of adsorbates can be evaluated using the equation

$$E_f{}^{d} = E^{nA/G-d} - E^{nA/G} - \Delta N\mu(C) \quad (3)$$

The first term ($E^{nA/G\text{-}d}$) in this equation corresponds to the total energy of n × A adsorbed on graphene with d-type (DV or SW in this study) defects, and the second term is the total energy of n × A adsorbed on pristine graphene. ΔN is the difference in the number of C atoms between the graphene with defects and pristine graphene, that is #C (defected graphene) − #C (pristine graphene). For SW and DV, ΔN is equal to 0 and −2, respectively. The changes in defect formation energies with increasing surface functionalization can be quantified from the difference in the energies of varying adsorbate concentrations with those of the adsorbate-free cases. For evaluating the changes in vibrational frequencies as a function of strain, topological defects, and adsorbates, we used the finite displacement method implemented in the VASP package. The method allows for determination of the Hessian matrix (i.e., the matrix of the second derivatives of the energy with respect to the atomic positions) and therefore the vibrational frequencies of the system. Each ion was displaced in the direction of each Cartesian coordinate, allowing the Hessian matrix to be determined from the resulting forces. We have used central differences where each ion was displaced in each direction by positive and negative displacements of 0.015 Å in size. For evaluating the strain effect on the vibrational frequencies of pristine graphene, biaxial strain (both compressive and tensile) was applied up to 2%.

3. EXPERIMENTAL RESULTS AND DISCUSSION

Raman measurements were performed as a function of electrochemical cycling for the G-Si samples. A systematic evolution of the graphene Raman spectrum was observed, as shown in Figures 1 and 2. The "0" spectrum shows the Raman peaks of the as-prepared CVD grown graphene transferred on the Si(111) substrate (G-Si-0). The following first-order peaks and higher order overtones were observed in order of decreasing intensity: 2D (~2700 cm^{-1}), G (~1600 cm^{-1}), D + D′′ (~2470 cm^{-1}), 2D′ (~3250 cm^{-1}), and D (~1350 cm^{-1}). These peaks are representative of typical CVD grown

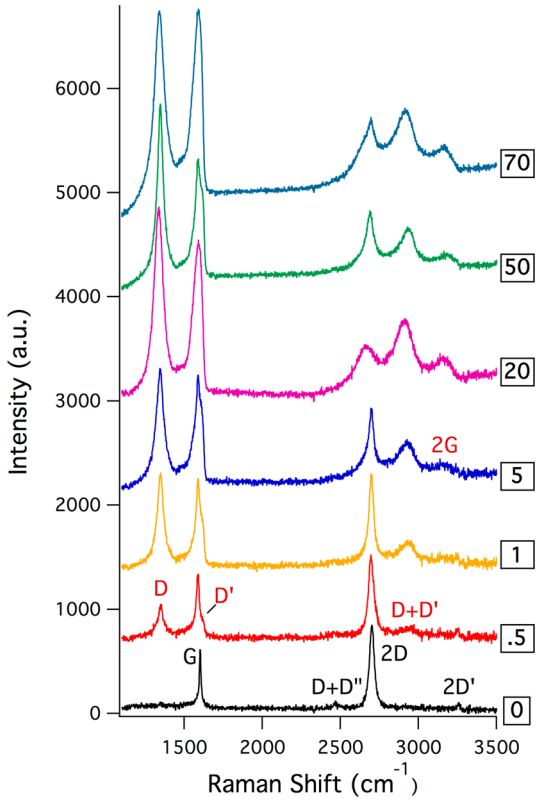

Figure 1. Ex situ Raman measurements of a series of electrochemically cycled samples of monolayer graphene transferred on Si(111); 0 indicates the Raman spectrum of the as-prepared sample prior to any cycling, and 0.5−70 indicate average spectra for six samples that have been cycled at different conditions ranging from single lithiation (0.5) to 70 lithiation-delithiation cycles (70). The spectra are offset for viewing clarity. Peaks labeled in black are present in the as-prepared samples, while the ones labeled in red appear during different stages of cycling. The spectra show an increase in the defectivity of the graphene monolayer with increasing number of cycles, but this effect saturates for higher numbers of cycles.

monolayer graphene with a low level of defectivity[32] as observed from the high 2D/G ratio and low intensity of the D peak. The D and D′ peaks are attributed to disorder-mediated first-order scattering. The 2D and 2D′ peaks are overtones of the D and D′ peaks, respectively. The 2D and 2D′ peaks originate from a process where momentum conservation is satisfied by two phonons with opposite wave vectors, so no defects are required for their activation. They can thus be used as an indirect measure of the extent of nondefective graphene present in the Raman cross-section. The G peak is a result of in-plane optical vibrational modes of the sp^2-hybridized carbon atoms. Because absolute intensity measurement is a difficult task in Raman spectroscopy, the normalized intensity I(D)/I(G) ratio is widely used to measure the amount of disorder.[46]

After a single lithiation (G-Si-0.5), the Raman spectrum 0.5 showed a marked increase in I(D), and an additional defect peak, D′, appeared as a shoulder on the G peak. The evolution of the D and D′ features imply the development of graphene defects upon lithiation. This early stage defect formation has been reported previously for copper substrates[39] and graphitic carbon.[47] A broad D + D′ peak at ∼2930 cm^{-1} also appeared at this stage. The I(2D), however, remained relatively unaffected. For the case of 1 and 5 cycles, the D, D′, and D + D′ peaks continued to grow, and simultaneously, the 2D peak started to decrease. I(G) also increased slightly, and by the fifth cycle, both the I(D) and I(G) were comparable to each other and higher than I(2D). Additionally, by the fifth cycle, a broad peak was visible around ∼3170 cm^{-1}, which is indicative of the second-order overtone of the G peak (i.e., the so-called 2G peak) as observed for Raman spectrum 5. We confirmed the identity of this 2G peak by a lack of dispersion in its peak position with different laser energies.[46] The 2G peak represents a double resonant process that is typically absent in graphene but has been observed commonly in chemically defective forms of graphene such as graphene oxide.[48] Overall, as the electrochemical cycling proceeded from 0.5 to 5 cycles, the Raman spectra showed increasing defectivity in the graphene film.

After the fifth cycle, additional electrochemical cycling had relatively minimal effects on the Raman spectrum. This cycling behavior suggests that the defectivity in the graphene monolayer resulting from electrochemical cycling was limited to the initial lithiation stages and only caused partial damage to the graphene layer. The different conditions examined can thus be categorized into two phases of the process based on the evolution of the different peaks: the first phase (up to 5 cycles), characterized by significant changes in the Raman peaks for relatively small advances in the electrochemical cycling, and the second phase (20−70 cycles), characterized by relatively small changes, almost plateauing, in the Raman peak intensities for a large number of cycles.

Figure 2 provides quantitative analyses based on the spectra in Figure 1. Figure 2a shows the change in peak heights of the main peaks, namely the G, 2D, D, and D′ peaks, as a function of the number of electrochemical cycles. A double exponential fit to the peak heights shows a rollover in all cases for higher numbers of cycles. The I(2D) drops by ∼50% at the 20th cycle and is then relatively unaffected by further cycling. I(D) and I(D′) peaks increase significantly up to ∼20 cycles and then also stabilize. The variations observed at the higher number of cycles for the defect peaks were attributed to nonuniformities in the galvanostatic cycling process and sample-to-sample variation. The G peak also became relatively stable at a higher number of cycles after an increase of 50% in the first cycle. Because I(G) is expected to decrease with increasing defect density,[49] the increase in I(G) is not likely to be due to defect formation. Doping is more likely the cause because a change in the Fermi level excludes part of the Brilluoin zone from contributing and reduces the destructive interference, thereby causing I(G) to increase.[32] Previous experiments have found similar increases in I(G) due to a 0.5 V electrochemical potential,[50] which corresponds to charge density of ∼10^{13} cm^{-2}.[51]

Figure 2b shows the I(D)/I(G) ratio as a function of cycling. This ratio showed a similar trend as observed for the individual peaks, with a saturation value of ∼1.5−2.0. Interestingly, the I(D)/I(G) saturation value was similar to that reported for rGO following solvothermal reduction of graphene oxide,[27] suggesting that the level of defectivity at the later stages of cycling is comparable to that of rGO. Previous reports of I(D)/I(G) for monolayer graphene as a function of Ar^+ ion bombardment (vacancy type defect)[35] and oxidation (functionalization type defect)[52] have shown a transition from a low defect to a high defect regime, which was characterized by an initial increase in the I(D)/I(G) ratio in the low defect regime followed by a strong decrease in the ratio in the high defect regime. The low and high defect regimes are referred to as

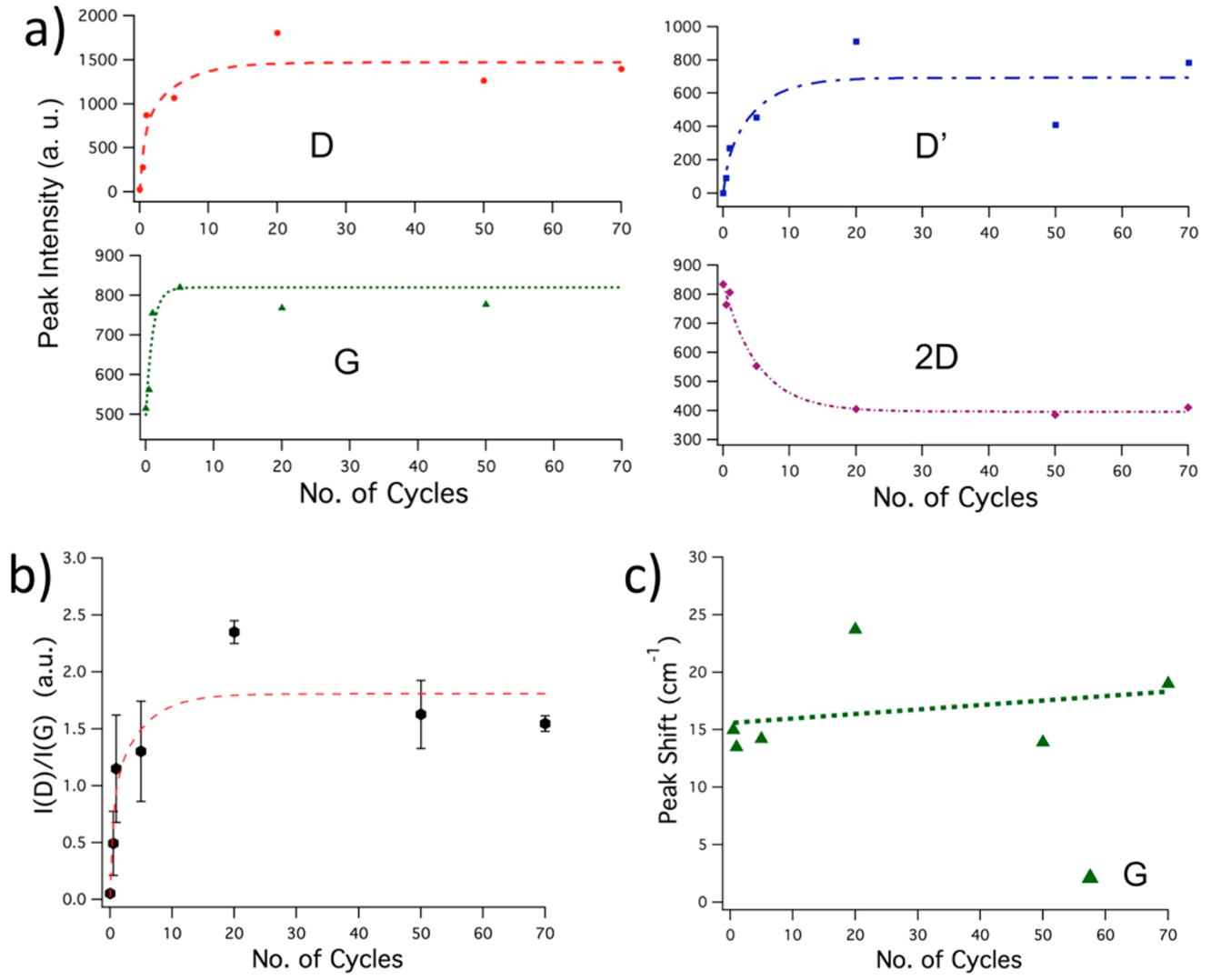

Figure 2. Analysis of the ex situ Raman measurements. (a) Peak intensity (peak height) for the D, G, 2D, and D′ peaks as a function of the number of electrochemical cycles. The dotted lines are drawn as a guide to the eye using double exponential fits for each peak, showing the early stage of increasing defectivity followed by a rollover to a later stage of nearly constant defectivity. (b) I(D)/I(G) ratio as a function of the number of electrochemical cycles, showing a similar trend as that of the individual peaks. I(D)/I(G) saturates to ∼1.5−2, with a corresponding 50% drop in I(2D). Also shown is the standard deviation of the I(D)/I(G) showing higher area-to-area variation at the early stages of cycling compared to the later stage. (c) Red shift for the G peak after cycling with respect to its initial position prior to cycling (i.e., Raman $\text{shift}_{\text{as-prepared}}$ — Raman $\text{shift}_{\text{x-cycles}}$).

Stage 1 (graphene to nanocrystalline graphene) and Stage 2 (nanocrystalline sp^2 to low amorphous sp^3), respectively. This transition was reported to be between I(D)/I(G) ∼3−4, which is significantly higher than the value observed in our case, indicating that the final defect density in the second phase was still in Stage 1 at the saturation value. Further evidence that the samples remained in Stage 1 is the fact that I(2D) saturated at ∼50% and did not continue to drop as is expected for Stage 2.[52] Using the phenomenological model proposed by Lucchese et al.[53] for ion bombardment induced defects in monolayer graphene, we can make an approximate estimate for the average defect distance in our case to be ∼6−8 nm. It should be noted that this model is developed for the case of vacancy type defects and does not account for functionalization type defects, both of which may be present in our case.

Figure 2b also shows the standard deviation in measuring several spots on each sample, which is attributed to the area-to-area variation in the Raman signal. A relatively high spatial variation is observed at the early stages of cycling, while the spatial variation reduces as the peak intensities saturate for higher numbers of cycles. Figure 2c shows the shift in the peak positions for the G peak with electrochemical cycling. The G peak shows a distinct redshift of ∼15 cm^{-1} upon the first lithiation and then only a marginal additional shift for higher numbers of cycles. Because defect-induced shifts in the G peak is minimal in Stage 1 in comparison with those in Stage 2,[49] and doping induces stiffening of Raman modes,[51] we hypothesize that strain-induced shifts may be dominant, as discussed below in the first-principles modeling results. The strain could be the result of the large volume change and resulting amorphization of the silicon substrate underneath the graphene film, as well as SEI formation on the surface of the graphene monolayer. A peak at ∼1550 cm^{-1} was also observed, which shows a greater than 5-fold increase in the peak height and area by the 70th cycle (Figure S4, Supporting Information). We attribute this peak to disordered carbon[54] from the SEI layer, which continues to grow with increasing numbers of cycles. It is likely that the presence of a thicker SEI limits exposure of the

graphene layer to the reactive electrolyte species and perhaps alleviates the defects formed due to this exposure.

In Figure S1b (Supporting Information), the approximate amount of charge (equivalently the lithium exposure) required to create defects in the graphene monolayer was estimated. This calculation assumes an ideal case of uniform lithiation and perfect graphene coverage over the entire surface of the silicon substrate. Our estimate indicates that an exposure ≥0.2−0.3 C/mm^2 will result in defect levels comparable to the saturation value. This value provides a more universal estimate based on lithium exposure independent of the specifics of the cycling conditions.

Because chemical functionalization is likely to be a contributor to the observed changes in the Raman spectra, additional measurements were performed using an Ar-atmosphere Raman system to confirm these findings and show that the defectivity is not affected by oxidative processes as a result of air exposure. Figure 3 shows the Ar-atmosphere

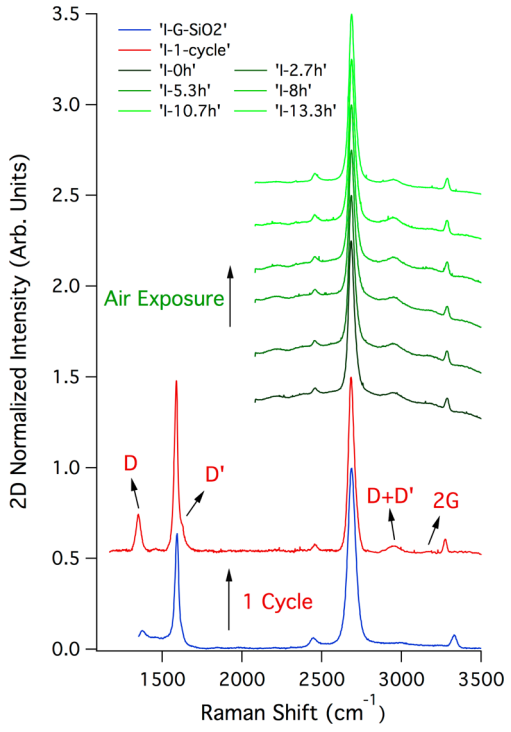

Figure 3. Ar-atmosphere Raman measurements of a G-SiO_2 sample before and after one CV cycle showing similar trends as the ex situ single lithiation (0.5) case. Graphene peaks that appear after the cycling are indicated in red. A series of plots are collected after the first CV cycle as the cell is exposed to air (shown in green) to show that air exposure does not change the Raman spectrum.

Raman spectroscopy data of a G-SiO_2 substrate following the first cycle voltammetry. Similar to the ex situ G-Si-0.5 sample, the Raman spectrum shows new defect-related features after the cycling and analogous evolution of the existing features. Figure S2c, Supporting Information shows the effect of more cycling (3 electrochemical cycles) on the Raman spectrum of the G-SiO_2 substrate. As expected, more cycling results in more pronounced evolution of the D′ peak and an increase in the intensity of the D peak, similar to the G-Si-1 case. Figure 3 also shows that the 2D region of the spectra is nearly invariant over 14 h, which further confirms that air exposure postcycling did not affect the Raman measurements.

Additionally, we transferred graphene to an H-terminated Si substrate and cycled the as-grown graphene on Cu foil (G-Cu) (Figure S3a,b, Supporting Information). For both of these substrates, a negligible amount of oxygen is present on the substrate surface and hence at the interface between the graphene and substrate. The defect footprint in both cases was similar to that of the G-Si samples suggesting that the native silicon oxide in the case of the G-Si samples was not the sole source of oxygen functionalization. The level of defectivity in the graphene monolayer for the G-Cu sample was, however, much lower than its G-Si-20 counterpart, presumably due to the difference in the substrate lithiation capacities.

Overall, the graphene monolayer remains partially intact and shows a distinct graphene signature in Raman spectra following several electrochemical cycles. The changes in the Raman spectra with electrochemical cycling are likely due to the evolution of preexisting defects and the chemical functionalization of the graphene due to interaction with Li and other species such as O and F. In particular, partially fluorinated[55] and oxidized[56] graphene sheets have shown similar Raman features as the electrochemically cycled graphene, which also points to a functionalization-defect interplay. In the next section, this interplay between chemical functionalization and defect evolution is further explored with DFT modeling.

4. COMPUTATIONAL RESULTS AND DISCUSSION

The observed changes in Raman spectra described in the previous section can be attributed to a multitude of complex, possibly interacting, factors including topological defect creation, chemical functionalization, lithium adsorption, and strain induced by electrochemical cycling. In the following section, we start with DFT studies of each individual factor that has been shown previously, and building on this, we present a study of the interaction between chemical functionalization and defect creation. We use simplified models to investigate the various factors, as the simulation of the time evolution of the full system with solvent under electrochemical cycling is currently not feasible. Nonetheless, qualitative results obtained from these models give insights into the effects of different mechanisms on the measured Raman spectra.

The electronic properties of graphene can be tuned by doping or edge chemical modification. Adsorption on graphene can also lead to changes in its properties, and among different ad-species, Li, F, and O are of significant interest in the aforementioned electrochemical experiments. Li, in particular, is evidently important for applications in Li-ion batteries. In addition, O and F are common elements in the SEI. The emergence and changes in the intensity of the D peak in the Raman spectra during electrochemical cycling indicate continual changes in the defect density.[52,57] The nature of the defects, whether sp^3 in character (e.g., functionalization with F or O) or topological defects in the honeycomb lattice (e.g., vacancies or Stone−Wales defects) can also be inferred from the ratios of D and D′ intensities in the Raman spectrum.[58] However, the effects of a metallic ad-species such as Li or the combination of adsorption/functionalization and topological defects on Raman frequencies have not been previously investigated. In this section, we explore the effect of Li, O, and F on the vibrational frequencies and the defect formation energies in the presence of topological defects. We specifically explore SW and DV topological defects; the former has the lowest formation energy compared to other topological defects, while the latter is thermodynamically favored, and the

most common type of vacancy defect observed experimentally. DV was also shown to significantly lower the Li penetration barrier through graphene.[17,22] Although the formation energies of these defects are high, they were chosen as representative structures for evaluating the aforementioned effects of adsorption/functionalization.

DFT calculations were performed for various configurations of Li, F, and O adsorption on graphene both with and without topological defects. The lowest energy adsorption sites were different for all considered elements, and Li, F, and O were relaxed to hollow, top, and bridge sites, respectively (Figure 4 and Figure S5a–c, Supporting Information). Upon adsorption, Li donates part of its charge to the more electronegative C atoms in its proximity, giving rise to the doping-induced changes in the Raman spectra discussed above. The charge accumulation occurs between Li and C atoms, while depletion was observed above Li and in between the nearest C–C ring atoms (Figure 5). The interaction between Li and graphene was clearly of a highly ionic character, although it should be noted that the structural changes associated with Li adsorption were relatively small. The placement of a single F on the top site of C resulted in a reduction of electron density on graphene due to the higher electronegativity of F with respect to C. As a result, the nearest C–C bonds were enlarged from 1.42 to1.48 Å. For higher F concentrations, double side adsorption was found to become favorable and the enlargement of C–C bonds was >1.55 Å, suggesting that F adsorption leads to local distortion in the honeycomb lattice. This effect was further enhanced in the presence of topological defects.

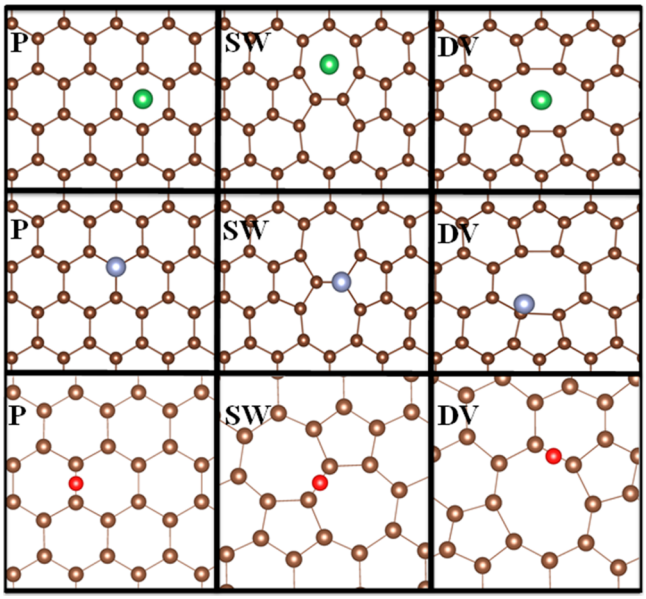

Figure 4. Lowest adsorption energy configurations of isolated Li, F, and O on pristine graphene and graphene with SW and DV defects. Green, gray, red, and brown balls represent Li, F, O, and C atoms, respectively.

Similarly, for O adsorption, electrons were drained from the bridge C–C bond and accumulated on the newly formed C–O bond. Accordingly, an expansion of the C–C bridge of about 0.1 Å in all bonds after the attachment of a single oxygen atom was observed. Further increasing the concentration showed that double-sided adsorption was also preferable (Figure S5c, Supporting Information). Overall, compared to Li, lattice distortions induced by the adsorbates in graphene were more pronounced for F and O, resembling a more sp^3-like carbon bonding. F on top of the C atom led to local structural distortion of the honeycomb lattice in which the C atom was pulled away from the flat graphene sheet. Likewise, the C–C bridge was distorted in the case of O attachment. However, if a counter O was placed directly below the adsorption site, out-of-plane displacements were minimal. In defected structures, starting with the introduction of a second O, carbon–carbon separation (>1.7 Å) was also observed.

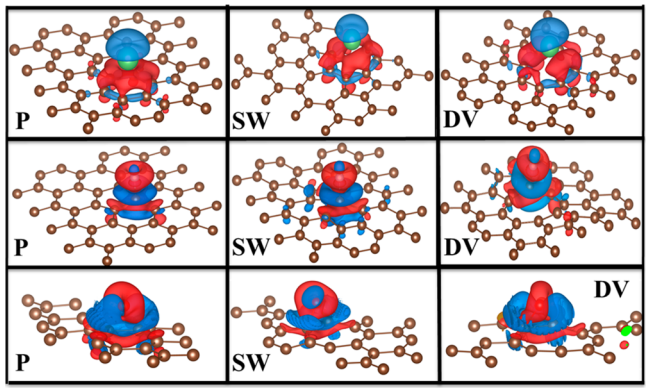

Figure 5. Changes in charge density upon adsorption of (top to bottom) Li, F, and O on (left to right) pristine graphene (P) and graphene with SW and DV defects. The charge density differences are obtained by subtracting the electron densities of the isolated Li, F, O, and graphene alone from those of the charge densities of the adsorbed systems. The charge densities of the isolated systems are calculated without further relaxation. Red colored areas represent charge accumulation, while blue corresponds to charge depletion.

Apart from the structural, bonding, and electronic changes described above, topological defects can also be modified by adsorption/functionalization. Therefore, in an effort to understand the effect of adsorbed species on defect evolution, the changes in defect formation energies were calculated for the graphene layer in the presence of Li, F, and O using the total energies of the most stable configurations identified in the previous section. The procedure for calculating the change in defect formation energies is described in the Experimental and Computational Methods section.

As shown in Table 1, these calculations show that increasing coverage of adsorbed Li, F, and O gradually reduces the formation energies of topological defects. The reduction in the defect formation energy was about 1.6 eV (SW) and 2.5 eV (DV) from no adsorbate to the highest Li coverage of 0.1 monolayer. In the case of F, these values become 1.6 and 1.9 eV, respectively, while in the case of O, the reduction was larger with 2.1 eV for SW and 5.4 eV for DV defects and was highly coverage-dependent. This coverage dependence was likely affected by the substantial structural modification introduced by O adsorption, in which C–C bond breaking was observed. In fact, the final structures for the highest O coverage were qualitatively different from the initial defect configurations. The fact that we find topological defects to become likely at high O coverage is consistent with previous work that found that O leads to cleavage of graphene.[25,26]

Motivated by these considerations and the observed shifts in the Raman spectra, the role of functionalizing agents on the vibrational frequencies was also explored. In Figure S6a–l (Supporting Information), we show the vibrational frequencies calculated for one-sixth monolayer-equivalent of Li, F, and O

Table 1. Adsorbate-Induced Defect Formation Energies (eV) of SW and DV Defects in the Presence of Li, F, and O of Varying Concentrations[a]

		Li			F			O		
	clean	1	2	3	1	2	3	1	2	3
SW	4.7 (3.6)	4.2	3.2	3.1	3.9	3.3	3.2	3.1 (2.7)	2.8 (2.1)	2.6 (0.94)
DV	6.8 (5.6)	5.8	4.5	4.3	5.9	5.7	4.9	5.1 (4.3)	3.3 (2.5)	1.4 (0.28)

[a]Values are given for calculations on 4 × 4 supercells, except the ones in parentheses, which are from 3 × 3 supercells.

on pristine graphene, graphene with SW defects, and graphene with DV defects. It should be noted that in the presence of defective graphene, the identification of the G peak position was not possible in our calculations. The associated eigenvectors of the vibrational modes are heavily modified, as our computational cell presents a high defect density. Nevertheless, by studying the vibrational frequencies of the defective graphene structures with and without the adsorbates, we determine what changes can be expected in the vibrational frequencies of pristine graphene when these topological defects are present and when they interact with adsorbates such as Li, O, and F.

The overall trend in the changes observed for the vibrational frequencies for pristine graphene can be attributed to the changes introduced in the graphene lattice structure and the C−C bond lengths that are induced by different adsorbates. In the case of O adsorption on the surface of pristine graphene, oxygen atoms create a dampening effect on the in-plane motion of carbon atoms on both sides of the bridge position. The bond lengths are generally shorter between these C atoms, which may explain the slightly higher wavenumber (1582 cm^{-1}) for this mode compared to the value calculated for pristine graphene (1565 cm^{-1}). Similar to O, when graphene is functionalized with F atoms, there is local structural distortion in the graphene lattice. The resulting stiffer C−C bond induces a stiffer vibrational frequency obtained for the highest frequency mode (1571 cm^{-1}) compared to that of pristine graphene. Li-functionalized graphene, on the other hand, presents a different effect than those obtained for O and F. Li adsorption leads to nearly uniform softening of the C−C bond lengths throughout the graphene lattice. This softening effect of Li on the C−C bond lengths resembles that induced by tensile strain. In particular, the highest vibrational frequency mode was found to be softer than that of adsorbate-free graphene, with a lower wavenumber of 1518 cm^{-1}.

For graphene with topological defects, additional higher vibrational frequency modes with wavenumbers of 1813 and 1696 cm^{-1} are found for DV and SW defects, respectively (Figure S7, Supporting Information). These high frequency modes can be attributed to the stiffer C−C bonds in these defective structures. In the presence of O, Li, and F, the vibrational modes of these defective graphene structures are further modified. In particular, when functionalized with three O atoms, the highest vibrational frequencies are reduced to 1719 and 1623 cm^{-1} for DV and SW, respectively. The large elongation induced in the C−C bonds due to the functionalization is reflected as the softening of the highest vibrational frequency modes found for the adsorbate-free defective graphene. The functionalization of the defective graphene with three F atoms produces a similar effect as oxygen. The preferred adsorption configuration for F atoms is on top of C sites near the defect regions, and similar to oxygen, fluorine induces significant enlarging in the neighboring C−C bonds that is more enhanced in the case of the DV defect. Specifically, the highest vibrational frequencies are reduced to 1722 and 1651 cm^{-1} for DV and SW defects, respectively. The change induced by the adsorbates on the defective graphene structure is smaller in the case of Li compared to F and O. The adsorption configuration of three Li atoms is double sided, on top and near defect sites. In this case, the highest vibrational frequencies are reduced to 1746 and 1665 cm^{-1} for DV and SW defects, respectively. A more detailed discussion is provided in the Supporting Information. In short, while topological defects introduce higher frequency modes than in pristine graphene, the interaction between these defects and functionalization reduces the frequencies of these modes.

Given the significant expansion of the Si(111) substrate during cycling and the functionalization and growth of SEI on the surface of the monolayer graphene, it is also important to consider the contribution of strain in this scenario. While the strain geometry evolution during the cycling is likely to be complex, we approximated a situation of biaxial strain[33] to simulate the conditions and understand the effect of strain on the Raman spectra. The changes in the vibrational frequencies of the pristine graphene were calculated under applied biaxial strain, both compressive and tensile up to 2% (Figure S7, Supporting Information) to assess the G peak dependence on strain. These results suggest that the applied tensile strain (presented by positive percentages in the figure) gradually softens the vibrational frequency associated with the G peak from 1565 cm^{-1} (for zero strain) to 1537, 1508, and 1453 cm^{-1} for 0.5, 1, and 2% strain, respectively, resulting from less stiff in-plane C−C bonds in the tensile strained graphene. These results are consistent with previous DFT studies of strain-induced vibrational frequency shifts in graphene[59,60] and suggest that the initial red shift (15 cm^{-1}) observed in the G peak experimentally upon lithiation and the continuing shift are consistent with graphene undergoing tensile strain.

While it is not possible in such a complex environment to pinpoint specific cause-effect, our modeling results suggest that a combination of defect formation, functionalization, and tensile strain are likely contributing to the experimentally observed modification of the Raman spectra during electrochemical cycling. Our results indicate that oxygen adsorption promotes the creation of topological defects, and the only source of oxygen is electrolyte decomposition. The fact that defect creation as observed via Raman saturates after ∼10 cycles may be related to the suppression of electrolyte decomposition after a stable SEI is formed.

5. CONCLUSIONS

In summary, we have performed a detailed Raman study for monolayer graphene on Si(111) and corresponding DFT modeling of free-standing graphene to explore how the structure of the graphene layer evolves in the Li-ion battery environment over extended electrochemical cycling. Most importantly, the graphene monolayer remains partially intact,

and the defectivity saturates at I(D)/I(G) ~1.5−2 after the early stages of cycling, and longer cycling periods have minimal additional impact. Using Ar-atmosphere Raman measurements, these findings were confirmed and show that the defectivity is not affected by air exposure during ex situ measurement conditions. Because previous approaches have suggested that Li diffusion through the basal plane of graphene is only possible through defect sites, DFT modeling was employed to understand how the Li-ion environment could potentially induce additional defects, which would facilitate Li-ion diffusion through the graphene layer. This modeling showed that defects can act as active sites for adsorbates (Li, O, and F) and that chemical functionalization can lower the defect formation energies. In this respect, active sites with specific adsorbates can form nuclei for extended defects. The modified Raman spectra and calculations thus suggest that the observed increasing level of defectivity can be attributed to a combination of vacancy formation and chemical functionalization of the graphene as a result of interaction with Li and other atomic species such as O and F in the electrolyte. The defectivity level plateaus with further electrochemical cycling due to the suppression of interaction with chemical species in the electrolyte upon sufficient SEI formation on the graphene surface. Overall, this work provides quantitative insight into the structural evolution of graphene during electrochemical cycling and thus will inform ongoing efforts to employ graphene as an additive or coating in advanced Li-ion battery electrodes.

■ ASSOCIATED CONTENT

Ⓢ Supporting Information

Optical image of G-SiO_2; galvanostatic and CV cycling data; additional ex situ and Ar-atmosphere Raman spectra and analyses; atomistic configurations of Li, F, and O adsorption on graphene with and without topological defects; and vibrational frequencies and effects of defects and adsorbates as calculated from DFT. This material is available free of charge via the Internet at http://pubs.acs.org.

■ AUTHOR INFORMATION

Corresponding Author

*E-mail: m-hersam@northwestern.edu.

Author Contributions

○These authors contributed equally to the manuscript. The manuscript was written through contributions of all authors. All authors have given approval to the final version of the manuscript.

Notes

The authors declare no competing financial interest.

■ ACKNOWLEDGMENTS

This research was supported as part of the Center for Electrical Energy Storage, an Energy Frontier Research Center funded by the U.S. Department of Energy, Office of Science, Office of Basic Energy Sciences (Award Number DE-AC02-06CH11357). Use of the Center for Nanoscale Materials at Argonne National Laboratory was supported by the U.S. Department of Energy, Office of Science, Office of Basic Energy Sciences (Contract Number DE-AC02-06CH11357). Battery testing instrumentation was funded by the Initiative for Sustainability and Energy at Northwestern University (ISEN). This research made use of the NUANCE Center at Northwestern University, which is supported by the NSF-MRSEC (NSF DMR-1121262), Keck Foundation, and the State of Illinois. K.P. thanks Dr. Gosztola at the Center for Nanoscale Materials for assistance with Raman spectroscopy. L.J. and K.P. thank Dr. Josh Wood for useful discussions and Dr. EunKyung Cho and Dr. James Johns for assistance with graphene transfer on H-terminated silicon samples.

■ REFERENCES

(1) Chen, P.; Su, Y.; Liu, H.; Wang, Y. Interconnected Tin Disulfide Nanosheets Grown on Graphene for Li-Ion Storage and Photocatalytic Applications. *ACS Appl. Mater. Interfaces* **2013**, *5*, 12073−12082.

(2) Ye, Y.-S.; Xie, X.-L.; Rick, J.; Chang, F.-C.; Hwang, B.-J. Improved Anode Materials for Lithium-Ion Batteries Comprise Non-Covalently Bonded Graphene and Silicon Nanoparticles. *J. Power Sources* **2014**, *247*, 991−998.

(3) Yang, S.; Gong, Y.; Liu, Z.; Zhan, L.; Hashim, D. P.; Ma, L.; Vajtai, R.; Ajayan, P. M. Bottom-up Approach toward Single-Crystalline VO_2-Graphene Ribbons as Cathodes for Ultrafast Lithium Storage. *Nano Lett.* **2013**, *13*, 1596−1601.

(4) Chen, P.; Guo, L.; Wang, Y. Graphene Wrapped SnCo Nanoparticles for High-Capacity Lithium Ion Storage. *J. Power Sources* **2013**, *222*, 526−532.

(5) Zhou, X.; Wan, L.-J.; Guo, Y.-G. Binding SnO_2 Nanocrystals in Nitrogen-Doped Graphene Sheets as Anode Materials for Lithium-Ion Batteries. *Adv. Mater.* **2013**, *25*, 2152−2157.

(6) Wei, W.; Yang, S.; Zhou, H.; Lieberwirth, I.; Feng, X.; Müllen, K. 3D Graphene Foams Cross-Linked with Pre-Encapsulated Fe_3O_4 Nanospheres for Enhanced Lithium Storage. *Adv. Mater.* **2013**, *25*, 2909−2914.

(7) Yang, S.; Yue, W.; Zhu, J.; Ren, Y.; Yang, X. Graphene-Based Mesoporous SnO_2 with Enhanced Electrochemical Performance for Lithium-Ion Batteries. *Adv. Funct. Mater.* **2013**, *23*, 3570−3576.

(8) Eom, K.; Joshi, T.; Bordes, A.; Do, I.; Fuller, T. F. The Design of a Li-Ion Full Cell Battery Using a Nano Silicon and Nano Multi-Layer Graphene Composite Anode. *J. Power Sources* **2014**, *249*, 118−124.

(9) Jang, B. Z.; Liu, C.; Neff, D.; Yu, Z.; Wang, M. C.; Xiong, W.; Zhamu, A. Graphene Surface-Enabled Lithium Ion-Exchanging Cells: Next-Generation High-Power Energy Storage Devices. *Nano Lett.* **2011**, *11*, 3785−3791.

(10) Zhao, X.; Hayner, C. M.; Kung, M. C.; Kung, H. H. Flexible Holey Graphene Paper Electrodes with Enhanced Rate Capability for Energy Storage Applications. *ACS Nano* **2011**, *5*, 8739−8749.

(11) Zhao, X.; Hayner, C. M.; Kung, M. C.; Kung, H. H. In-Plane Vacancy-Enabled High-Power Si-Graphene Composite Electrode for Lithium-Ion Batteries. *Adv. Energy Mater.* **2011**, *1*, 1079−1084.

(12) Sun, F.; Huang, K.; Qi, X.; Gao, T.; Liu, Y.; Zou, X.; Wei, X.; Zhong, J. A Rationally Designed Composite of Alternating Strata of Si Nanoparticles and Graphene: A High-Performance Lithium-Ion Battery Anode. *Nanoscale* **2013**, *5*, 8586−8592.

(13) Andersson, A. M.; Edström, K. Chemical Composition and Morphology of the Elevated Temperature SEI on Graphite. *J. Electrochem. Soc.* **2001**, *148*, A1100−A1109.

(14) Zhang, S.; Ding, M. S.; Xu, K.; Allen, J.; Jow, T. R. Understanding Solid Electrolyte Interface Film Formation on Graphite Electrodes. *Electrochem. Solid-State Lett.* **2001**, *4*, A206−A208.

(15) Das, D.; Kim, S.; Lee, K.-R.; Singh, A. K. Li Diffusion through Doped and Defected Graphene. *Phys. Chem. Chem. Phys.* **2013**, *15*, 15128−15134.

(16) Zhou, L.-J.; Hou, Z. F.; Wu, L.-M. First-Principles Study of Lithium Adsorption and Diffusion on Graphene with Point Defects. *J. Phys. Chem. C* **2012**, *116*, 21780−21787.

(17) Fan, X.; Zheng, W. T.; Kuo, J.-L. Adsorption and Diffusion of Li on Pristine and Defective Graphene. *ACS Appl. Mater. Interfaces* **2012**, *4*, 2432−2438.

(18) Lee, E.; Persson, K. A. Li Absorption and Intercalation in Single Layer Graphene and Few Layer Graphene by First Principles. *Nano Lett.* **2012**, *12*, 4624−4628.

(19) Garay-Tapia, A. M.; Romero, A. H.; Barone, V. Lithium Adsorption on Graphene: From Isolated Adatoms to Metallic Sheets. *J. Chem. Theory Comput.* **2012**, *8*, 1064−1071.
(20) Medeiros, P. V. C.; Mota, F. B.; Mascarenhas, A. J. S.; de Castilho, C. M. C. Bonding Character of Lithium Atoms Adsorbed on a Graphene Layer. *Solid State Commun.* **2011**, *151*, 529−531.
(21) Zheng, J.; Ren, Z.; Guo, P.; Fang, L.; Fan, J. Diffusion of Li^+ Ion on Graphene: A DFT Study. *Appl. Surf. Sci.* **2011**, *258*, 1651−1655.
(22) Yao, F.; Güneş, F.; Ta, H. Q.; Lee, S. M.; Chae, S. J.; Sheem, K. Y.; Cojocaru, C. S.; Xie, S. S.; Lee, Y. H. Diffusion Mechanism of Lithium Ion through Basal Plane of Layered Graphene. *J. Am. Chem. Soc.* **2012**, *134*, 8646−8654.
(23) Sofo, J. O.; Suarez, A. M.; Usaj, G.; Cornaglia, P. S.; Hernández-Nieves, A. D.; Balseiro, C. A. Electrical Control of the Chemical Bonding of Fluorine on Graphene. *Phys. Rev. B: Condens. Matter Mater. Phys.* **2011**, *83*, 081411.
(24) Leenaerts, O.; Peelaers, H.; Hernández-Nieves, A. D.; Partoens, B.; Peeters, F. M. First-Principles Investigation of Graphene Fluoride and Graphane. *Phys. Rev. B: Condens. Matter Mater. Phys.* **2010**, *82*, 195436.
(25) Li, Z.; Zhang, W.; Luo, Y.; Yang, J.; Hou, J. G. How Graphene Is Cut upon Oxidation? *J. Am. Chem. Soc.* **2009**, *131*, 6320−6321.
(26) Sun, T.; Fabris, S. Mechanisms for Oxidative Unzipping and Cutting of Graphene. *Nano Lett.* **2012**, *12*, 17−21.
(27) Bagri, A.; Mattevi, C.; Acik, M.; Chabal, Y. J.; Chhowalla, M.; Shenoy, V. B. Structural Evolution during the Reduction of Chemically Derived Graphene Oxide. *Nat. Chem.* **2010**, *2*, 581−587.
(28) Ji, L.; Tan, Z.; Kuykendall, T. R.; Aloni, S.; Xun, S.; Lin, E.; Battaglia, V.; Zhang, Y. Fe_3O_4 Nanoparticle-Integrated Graphene Sheets for High-Performance Half and Full Lithium Ion Cells. *Phys. Chem. Chem. Phys.* **2011**, *13*, 7170−7177.
(29) Wang, B.; Li, X.; Zhang, X.; Luo, B.; Jin, M.; Liang, M.; Dayeh, S. A.; Picraux, S. T.; Zhi, L. Adaptable Silicon-Carbon Nanocables Sandwiched between Reduced Graphene Oxide Sheets as Lithium Ion Battery Anodes. *ACS Nano* **2013**, *7*, 1437−1445.
(30) Li, D.; Müller, M. B.; Gilje, S.; Kaner, R. B.; Wallace, G. G. Processable Aqueous Dispersions of Graphene Nanosheets. *Nat. Nanotechnol.* **2008**, *3*, 101−105.
(31) Li, X.; Zhu, Y.; Cai, W.; Borysiak, M.; Han, B.; Chen, D.; Piner, R. D.; Colombo, L.; Ruoff, R. S. Transfer of Large-Area Graphene Films for High-Performance Transparent Conductive Electrodes. *Nano Lett.* **2009**, *9*, 4359−4363.
(32) Ferrari, A. C.; Basko, D. M. Raman Spectroscopy as a Versatile Tool for Studying the Properties of Graphene. *Nat. Nanotechnol.* **2013**, *8*, 235−246.
(33) Ding, F.; Ji, H.; Chen, Y.; Herklotz, A.; Dörr, K.; Mei, Y.; Rastelli, A.; Schmidt, O. G. Stretchable Graphene: A Close Look at Fundamental Parameters through Biaxial Straining. *Nano Lett.* **2010**, *10*, 3453−3458.
(34) Mohiuddin, T.; Lombardo, A.; Nair, R.; Bonetti, A.; Savini, G.; Jalil, R.; Bonini, N.; Basko, D.; Galiotis, C.; Marzari, N.; et al. Uniaxial Strain in Graphene by Raman Spectroscopy: G Peak Splitting, Grüneisen Parameters, and Sample Orientation. *Phys. Rev. B: Condens. Matter Mater. Phys.* **2009**, *79*, 205433.
(35) Cancado, L. G.; Jorio, A.; Martins Ferreira, E. H.; Stavale, F.; Achete, C. A.; Capaz, R. B.; Moutinho, M. V. O.; Lombardo, A.; Kulmala, T. S.; Ferrari, A. C. Quantifying Defects in Graphene via Raman Spectroscopy at Different Excitation Energies. *Nano Lett.* **2011**, *11*, 3190−3196.
(36) Ryu, S.; Han, M. Y.; Maultzsch, J.; Heinz, T. F.; Kim, P.; Steigerwald, M. L.; Brus, L. E. Reversible Basal Plane Hydrogenation of Graphene. *Nano Lett.* **2008**, *8*, 4597−4602.
(37) Iqbal, M. W.; Singh, A. K.; Iqbal, M. Z.; Eom, J. Raman Fingerprint of Doping due to Metal Adsorbates on Graphene. *J. Phys.: Condens. Matter* **2012**, *24*, 335301.
(38) Pollak, E.; Geng, B.; Jeon, K.-J.; Lucas, I. T.; Richardson, T. J.; Wang, F.; Kostecki, R. The Interaction of Li^+ with Single-Layer and Few-Layer Graphene. *Nano Lett.* **2010**, *10*, 3386−3388.
(39) Radhakrishnan, G.; Cardema, J. D.; Adams, P. M.; Kim, H. I.; Foran, B. Fabrication and Electrochemical Characterization of Single and Multi-Layer Graphene Anodes for Lithium-Ion Batteries. *J. Electrochem. Soc.* **2012**, *159*, A752−A761.
(40) Wang, B.; Li, X.; Qiu, T.; Luo, B.; Ning, J.; Li, J.; Zhang, X.; Liang, M.; Zhi, L. High Volumetric Capacity Silicon-Based Lithium Battery Anodes by Nanoscale System Engineering. *Nano Lett.* **2013**, *13*, 5578−5584.
(41) Lee, W. J.; Hwang, T. H.; Hwang, J. O.; Kim, H. W.; Lim, J. W.; Jeong, H. Y.; Shim, J.; Han, T. H.; Kim, J. Y.; Choi, J. W.; et al. N-Doped Graphitic Self-Encapsulation for High Performance Silicon Anodes in Lithium-Ion Batteries. *Energy Environ. Sci.* **2014**, *7*, 621−626.
(42) Prado, M. C.; Jariwala, D.; Marks, T. J.; Hersam, M. C. Optimization of Graphene Dry Etching Conditions via Combined Microscopic and Spectroscopic Analysis. *Appl. Phys. Lett.* **2013**, *102*, 193111.
(43) Kresse, G.; Furthmüller, J. Efficient Iterative Schemes for Ab Initio Total-Energy Calculations Using a Plane-Wave Basis Set. *Phys. Rev. B: Condens. Matter Mater. Phys.* **1996**, *54*, 11169−11186.
(44) Kresse, G.; Joubert, D. From Ultrasoft Pseudopotentials to the Projector Augmented-Wave Method. *Phys. Rev. B: Condens. Matter Mater. Phys.* **1999**, *59*, 1758−1775.
(45) Perdew, J. P.; Ernzerhof, M.; Burke, K. Rationale for Mixing Exact Exchange with Density Functional Approximations. *J. Chem. Phys.* **1996**, *105*, 9982−9985.
(46) Jorio, A. Raman Spectroscopy in Graphene-Based Systems: Prototypes for Nanoscience and Nanometrology. *ISRN Nanotechnol.* **2012**, *2012*, 1−16.
(47) Sethuraman, V. A.; Hardwick, L. J.; Srinivasan, V.; Kostecki, R. Surface Structural Disordering in Graphite upon Lithium Intercalation/Deintercalation. *J. Power Sources* **2010**, *195*, 3655−3660.
(48) Vasu, K. S.; Chakraborty, B.; Sampath, S.; Sood, a. K. Probing Top-Gated Field Effect Transistor of Reduced Graphene Oxide Monolayer Made by Dielectrophoresis. *Solid State Commun.* **2010**, *150*, 1295−1298.
(49) Eckmann, A.; Felten, A.; Verzhbitskiy, I.; Davey, R.; Casiraghi, C. Raman Study on Defective Graphene: Effect of the Excitation Energy, Type, and Amount of Defects. *Phys. Rev. B: Condens. Matter Mater. Phys.* **2013**, *88*, 035426.
(50) Kalbac, M.; Reina-Cecco, A.; Farhat, H.; Kong, J.; Kavan, L.; Dresselhaus, M. S. The Influence of Strong Electron and Hole Doping on the Raman Intensity of Chemical Vapor-Deposition Graphene. *ACS Nano* **2010**, *4*, 6055−6063.
(51) Das, A.; Pisana, S.; Chakraborty, B.; Piscanec, S.; Saha, S. K.; Waghmare, U. V.; Novoselov, K. S.; Krishnamurthy, H. R.; Geim, A. K.; Ferrari, A. C.; et al. Monitoring Dopants by Raman Scattering in an Electrochemically Top-Gated Graphene Transistor. *Nat. Nanotechnol.* **2008**, *3*, 210−215.
(52) Eckmann, A.; Felten, A.; Mishchenko, A.; Britnell, L.; Krupke, R.; Novoselov, K. S.; Casiraghi, C. Probing the Nature of Defects in Graphene by Raman Spectroscopy. *Nano Lett.* **2012**, *12*, 3925−3930.
(53) Lucchese, M. M.; Stavale, F.; Ferreira, E. H. M.; Vilani, C.; Moutinho, M. V. O.; Capaz, R. B.; Achete, C. A.; Jorio, A. Quantifying Ion-Induced Defects and Raman Relaxation Length in Graphene. *Carbon* **2010**, *48*, 1592−1597.
(54) Chu, P. K.; Li, L. Characterization of Amorphous and Nanocrystalline Carbon Films. *Mater. Chem. Phys.* **2006**, *96*, 253−277.
(55) Nair, R. R.; Ren, W.; Jalil, R.; Riaz, I.; Kravets, V. G.; Britnell, L.; Blake, P.; Schedin, F.; Mayorov, A. S.; Yuan, S.; et al. Fluorographene: A Two-Dimensional Counterpart of Teflon. *Small* **2010**, *6*, 2877−2884.
(56) Yang, D.; Velamakanni, A.; Bozoklu, G.; Park, S.; Stoller, M.; Piner, R. D.; Stankovich, S.; Jung, I.; Field, D. A.; Ventrice, C. A., Jr.; et al. Chemical Analysis of Graphene Oxide Films after Heat and Chemical Treatments by X-Ray Photoelectron and Micro-Raman Spectroscopy. *Carbon* **2009**, *47*, 145−152.
(57) Tuinstra, F.; Koenig, J. L. Raman Spectrum of Graphite. *J. Chem. Phys.* **1970**, *53*, 1126−1130.

(58) Ferrari, A. C.; Robertson, J. Interpretation of Raman Spectra of Disordered and Amorphous Carbon. *Phys. Rev. B: Condens. Matter Mater. Phys.* **2000**, *61*, 14095−14107.
(59) Del Corro, E.; de la Roza, A. O.; Taravillo, M.; Baonza, V. G. Raman Modes and Grüneisen Parameters of Graphite Under Compressive Biaxial Stress. *Carbon* **2012**, *50*, 4600−4606.
(60) Rakshit, B.; Mahadevan, P. Absence of Rippling in Graphene Under Biaxial Tensile Strain. *Phys. Rev. B: Condens. Matter Mater. Phys.* **2010**, *82*, 153407.